A comparative study of internal kink stability in EU DEMO designs with negative and positive triangularity

Lina Zhou[1,a], Yueqiang Liu[2,a], Mattia Siccinio[3,4], Emiliano Fable[4], Tingting Wu[5], Taina Kurki-Suonio[6], Jari Varje[6], Deyong Liu[7]

1 College of Science, Dalian Maritime University, Dalian 116026, China
2 General Atomics, PO Box 85608, San Diego, CA 92186-5608, United States of America
3 EUROfusion Programme, Management Unit, Boltzmannstr 2, D-85748 Garching, Germany
4 Max-Planck-Institut für Plasmaphysik, Boltzmannstr. 2, 85748 Garching bei München, Germany
5 Southwestern Institute of Physics, PO Box 432, Chengdu 610041, China
6 Aalto Univ, Dept Appl Phys, POB 11000, FI-00076 Aalto, Finland
7 Department of Physics and Astronomy, University of California-Irvine, Irvine, CA 92697

a) Authors to whom any correspondence should be addressed.
E-mail: zhoulina@dlmu.edu.cn, liuy@fusion.gat.com

Abstract

Internal kink (IK) instability is investigated for EU DEMO plasmas in both negative and positive triangularity configurations. For negative triangularity (NT) plasmas, the IK becomes more unstable as an ideal conformal wall moves away from the plasma boundary, with the mode growth rate saturating at the wall radial location of about $b/a=1.5$, where a is the plasma minor radius and b the wall radial location. The plasma resistivity destabilizes the IK mode. The effect of sub-sonic toroidal plasma flow is sufficiently weak and can thus be ignored for these EU DEMO equilibria. These results are consistent with those for positive triangularity (PT) plasmas, albeit with larger mode growth rate in the NT configuration. Both perturbative and self-consistent magneto-hydrodynamic-kinetic hybrid calculations predict (partial) stabilization of the IK modes in both NT and PT configurations, with inclusion of various kinetic contributions. Precessional drift motion of trapped fusion-born alphas in EU DEMO produces weak stabilization to the IK mode. Stronger stabilization occurs with the toroidal precession of trapped thermal particles (ions and electrons) and the bounce-transit motion of thermal ions. The stabilization is similar between the NT and PT configurations, due to the similarity of the mode eigenfunction (occupying a nearly circular region in the plasma core) despite the sign difference in the triangularity. The non-perturbative MHD-kinetic hybrid

model predicts much less stabilization of the mode than the perturbative model, primarily due to the self-consistent determination of the mode eigenvalue in the former. Generally, no significant difference in the IK mode stability is found between the NT and PT plasmas in EU-DEMO.

Keywords: negative triangularity, drift-kinetic effect, internal kink instability, EU DEMO
(Some figures may appear in colour only in the online journal)

1. Introduction

Large-scale and low-frequency type-I edge localized modes (ELMs) are a ubiquitous feature of tokamak H-mode discharges [1], ejecting energy at levels that can cause material damage for the plasma-facing components in future large fusion devices such as ITER [2]. It has been estimated that bursting of type-I ELMs is sufficient to cause surface melting of the tungsten-coated target plates in European demonstration fusion reactor (EU DEMO), when the D-shaped plasma, i.e., a plasma with positive triangularity (PT), is operated in the so-called H-mode regime [3, 4]. Controlling large ELMs thus appears to be a critical design issue for fusion reactors operating in H-mode. Significant efforts have been devoted to investigating ELM-free regimes, either with ELMs suppressed by resonant magnetic perturbations [5-7] or naturally ELM-free regimes such as the QH-mode [8, 9], I-mode [10, 11], and also plasmas with negative triangularity (NT) shape [12-14].

The NT tokamak plasma, with the poloidal cross section exhibiting a reversed “D” shape, has become an increasingly attractive configuration for future fusion energy devices due to the absence of ELMs [15-18]. For instance, experiments on TCV have shown that global performance of the NT plasma can approach that of the H-mode regime with PT, thanks to lower transport levels [19]. Recent experiments in DIII-D simultaneously achieved the reactor-relevant plasma pressure ($\beta_N = 2.7$) and the H-mode confinement ($H_{98y2} = 1.2$), with low edge pressure and in the absence of ELMs [13]. Besides, an NT tokamak has other advantages in the heat deposition and construction economy, including a larger separatrix wetted area, more flexible divertor configuration design, wider trapped particle-free scrape-off layer, lower background magnetic field for internal poloidal field coils, and larger pumping conductance from the divertor room [12]. For these reasons, more research in both experiments and

modeling are needed on the NT configuration, and EU has been actively pursuing the venue of NT plasma scenarios for the DEMO design.

The EU DEMO represents the next step towards commercial fusion reactors following the ITER burning plasma experiments, according to the EU fusion roadmap [20, 21]. The EU DEMO design is a still on-going effort, with the baseline scenario designed in the PT configuration (DEMO-1). Recent design activities have considered the NT configuration as a potential candidate for EU DEMO, provided that the H-mode like confinement can be confirmed [4, 20]. These new NT (and correspondent PT) scenarios are based on the key equilibrium parameters of DEMO-1 and the equilibrium profiles calculated with the transport code ASTRA [22].

For the NT configuration, one essential research aspect is to analyze macroscopic MHD instabilities, such as the external (including the resistive wall mode) [16, 17] and internal kink modes. This work focuses on the internal kink (IK) study. The present EU DEMO plasma scenario design allows sawteeth, similar to the ITER design, despite the negative impact on the plasma core confinement. This is because the tokamak concept tends to accommodate as much plasma current as possible, since the overall confinement scales favorably with the plasma current. Large plasma current often leads to on-axis safety factor q_0 to be close or even below 1. The IK instability often occurs when the on-axis safety factor $q_0 < 1$. As far as the PT plasma is concerned, extensive research work has previously been devoted to studying various physics aspects associated with the IK instability, including the effect of the plasma resistivity [23], the ideal wall [24], as well as various kinetic effects from bulk ions [25], electrons [26], fast ions [27, 28] and fusion-born alphas [29, 30]. On the other hand, the IK mode in the NT configuration has so far been rarely studied [12, 31].

In this work, full toroidal modeling of the IK instability is carried out for the NT configuration in EU DEMO. Drift-kinetic effects on IK from both thermal particles and α-particles are investigated by utilizing the MHD-kinetic hybrid code MARS-K [32], following both perturbative and self-consistent approaches. We also investigate the effect of a conducting wall on the IK instability using the MARS-F code [33]. This is because the mode is located far away from the magnetic axis and close to the plasma boundary for these EU DEMO equilibria, which have very low q_0 values (~0.2) as compared to that in typical present day experiments. We note that q_0 can indeed evolve to such a low value in DEMO plasmas, due to the presence

of long-period "monster" sawtooth stabilized by a large fraction of energetic particles (EPs), in particular by fusion-born alphas [27, 34]. For comparison, we also perform modeling for the matching PT configuration in EU DEMO.

Section 2 briefly describes the MARS-F/K computational models. Section 3 reports the designed plasma equilibria with NT versus PT configurations in EU DEMO, and the IK stability study for these equilibria. Section 4 summarizes the results.

2. Computational models

For EU DEMO plasmas with NT versus PT shapes, the linear stability of the IK mode (both the eigenvalue and the eigenmode structure) is analyzed with the MARS-F/K codes [32, 35] that solve perturbed single fluid magneto-hydrodynamic (MHD) equations in full toroidal geometry. In the MARS-K formulation, the closure equation (for the perturbed plasma pressure) comes from the solution of the drift-kinetic equation for plasma particle species (both thermal and energetic particles). The MARS-K code has previously been successfully benchmarked against other codes [36, 37], and has been extensively utilized to study drift-kinetic effects on the IK modes [23, 26, 30], the external kink/resistive wall modes (EKMs/RWMs) [38-42] for PT plasmas, as well as the kinetic-feedback effects on EKMs/RWMs for NT plasmas [16, 17]. Detailed MARS-K/F formulations can be found from Refs. [32, 33]. Below we provide a brief description of the MARS-K model for completeness in understanding this work.

The main equations in the plasma region are written in the Eulerian frame

$$\left(\tilde{\gamma}+in\Omega\right)\boldsymbol{\xi}=\boldsymbol{v}+\left(\boldsymbol{\xi}\cdot\nabla\Omega\right)R^2\nabla\phi \tag{1}$$

$$\begin{aligned}\rho\left(\tilde{\gamma}+in\Omega\right)\boldsymbol{v}=&-\nabla\cdot\boldsymbol{p}+\boldsymbol{j}\times\boldsymbol{B}+\boldsymbol{J}\times\boldsymbol{b}\\&-\rho\left[2\Omega\hat{\boldsymbol{Z}}\times\boldsymbol{v}+\left(\boldsymbol{v}\cdot\nabla\Omega\right)R^2\nabla\phi\right]-R\Omega^2\nabla\cdot\left(\rho\boldsymbol{\xi}\right)\hat{\boldsymbol{R}}\end{aligned} \tag{2}$$

$$\left(\tilde{\gamma}+in\Omega\right)\boldsymbol{b}=\nabla\times\left(\boldsymbol{v}\times\boldsymbol{B}\right)+\left(\boldsymbol{b}\cdot\nabla\Omega\right)R^2\nabla\phi-\nabla\times\left(\eta\boldsymbol{j}\right) \tag{3}$$

$$\left(\tilde{\gamma}+in\Omega\right)p=-\boldsymbol{v}\cdot\nabla P \tag{4}$$

$$j=\nabla\times\boldsymbol{b} \tag{5}$$

$$\boldsymbol{p}=p\boldsymbol{I}+p_{\parallel}\hat{\boldsymbol{b}}\hat{\boldsymbol{b}}+p_{\perp}(\boldsymbol{I}-\hat{\boldsymbol{b}}\hat{\boldsymbol{b}}) \tag{6}$$

$$p_{\parallel} = \sum_j M_j v_{\parallel}^2 f_L^1 d\Gamma,\ p_{\perp} = \sum_j \frac{1}{2} M_j v_{\perp}^2 f_L^1 d\Gamma \qquad (7)$$

where ρ, $\boldsymbol{B}$ and $\boldsymbol{J}$ are the equilibrium plasma density, magnetic field and current density, respectively. P is the total equilibrium pressure (including that of thermal and energetic particle contributions). The perturbed quantities $\boldsymbol{\xi}$, $\boldsymbol{v}$, $\boldsymbol{b}$, $\boldsymbol{j}$, $\boldsymbol{p}$ represent the plasma displacement, perturbed velocity, magnetic field, current density and pressure, respectively. The (complex) eigenvalue $\tilde{\gamma}$ has the real and imaginary parts referring to the growth rate and mode frequency, respectively, of the modeled instability. The vectors $\hat{Z}$ and $\hat{R}$ are the unit vectors in the vertical and major radius directions, respectively, in the poloidal plane.

In the presence of the plasma equilibrium toroidal rotation, the eigenvalue is corrected by a Doppler shift frequency $in\Omega$ (plus other effects from the centrifugal and Coriolis forces as shown in Eq. (2)), with Ω being the angular frequency of the plasma flow along the geometric toroidal angle ϕ of the torus. Here, n is the toroidal mode number, assumed to be 1 in the present study. The plasma resistivity is denoted by η in Eq. (3), which is inversely proportional to Lundquist number $S = \tau_\eta / \tau_{\mathrm{A}}$, where τ_η and τ_{A} are the plasma current resistive diffusion time and the toroidal Alfven time, respectively. The Spitzer model is used for estimating the plasma resistivity, yielding the on-axis Lundquist number of $\sim 10^{10}$ for these EU DEMO plasmas. In this study, we assume the same plasma resistivity for NT and PT plasmas in order to make a fair comparison.

The drift-kinetic effects self-consistently enter the MHD equations via the perturbed kinetic pressure tensor $\boldsymbol{p}$ in Eq. (2). As shown in Eq. (6), the perturbed pressure tensor $\boldsymbol{p}$ consists of a scalar component p (the so-called adiabatic contribution to the perturbed pressure) and the anisotropic tensor components describing the non-adiabatic contributions. The tensor terms consist of components parallel ($p_{\parallel}$) and perpendicular ($p_{\perp}$) to the equilibrium field lines. The symbol $\boldsymbol{I}$ denotes the unit tensor here, and $\hat{\boldsymbol{b}} = \boldsymbol{B}/|B|$. The drift-kinetic pressure perturbations are calculated from Eq. (7), where Γ signifies the velocity space of the particles, and j represents the particle species, including the thermal ions and electrons as well as the fusion-born α-particles in this study. M_j is the corresponding particle mass. $v_{\parallel}$ and $v_{\perp}$ denote the parallel and perpendicular velocities of the particle guiding center drift motion, respectively. f_L^1 is the non-adiabatic perturbed distribution function as the solution of the drift-kinetic equation for

each particle species [32]. A key factor in the drift-kinetic solution is the mode-particle resonance operator [32]

$$\lambda_{ml} = \frac{n\left[\omega_{*N} + \left(\hat{\varepsilon}_k - \frac{3}{2}\right)\omega_{*T} + \omega_E\right] - \tilde{\omega}}{n\omega_d + \left[\alpha\left(m + nq\right) + l\right]\omega_b - i\nu_{eff} - \tilde{\omega}} \tag{8}$$

with ω_{*N} and ω_{*T} denoting the diamagnetic drift frequencies associated with the plasma density and temperature gradients, respectively. ω_E is the $\boldsymbol{E}\times\boldsymbol{B}$ drift frequency due to the equilibrium electrostatic potential. ω_d is the bounce-orbit-averaged toroidal precession drift frequency of particles, including the ω_E drift. ω_b is the particle bounce/transit frequency. $\hat{\varepsilon}_k$ is the particle kinetic energy normalized by temperature. $\tilde{\omega} = i\tilde{\gamma}$ is the (complex) mode frequency. l is the Fourier harmonic index over the particle bounce orbit. $\alpha = 1$ for passing particles, and $\alpha = 0$ for trapped particles. ν_{eff} is the effective particle collision frequency. Note that we assume a Maxwellian equilibrium distribution function for thermal particles, and an isotropic (in pitch angle) slowing-down (in energy) equilibrium distribution function for α-particles [43].

3. Numerical results

In what follows, we briefly introduce the plasma equilibria in sub-section 3.1, designed for EU DEMO with both NT and PT shapes. The effect of the wall resistivity on IK is weak for these equilibria. An ideal conformal wall is thus assumed in our investigations, with the MARS-F computational results reported in sub-section 3.2, while scanning the normalized wall minor radius b/a (with a being the plasma minor radius and b the wall radial location) and other plasma parameters. In sub-section 3.3, we investigate drift-kinetic effects on the IK mode following both perturbative and self-consistent approaches. There are two main differences between these two approaches. (i) The self-consistent approach allows modification of the eigenfunction of the IK mode by drift-kinetic effects, whilst the perturbative approach employs the eigenfunction calculated from the fluid theory to evaluate the perturbed drift-kinetic potential energy. (ii) In the self-consistent approach, the (unknown) growth rate of the IK mode enters into the drift-kinetic resonance operator, whilst the perturbative approach normally uses the (known) growth rate of the fluid IK for evaluating the resonance operator. Two extreme

cases of the ideal wall location are considered here, with the ideal wall placed (i) at the plasma boundary: b/a = 1, or (ii) far away from the plasma surface: b/a = 2.

3.1. Plasma equilibria for EU DEMO scenarios

Two pairs of plasma equilibria from the EU DEMO design, with drastically different plasma boundary shapes and different plasma currents I_p, are adopted in this study. Figure 1 compares the plasma boundary shapes for the four equilibria, plotted together with the assumed conformal vacuum vessel (VV) shape. The radial location *b/a* of the ideal conformal wall will be scanned in our study. The key equilibrium parameters with the NT shape (Fig. 1(a)) are: the plasma major radius $R_0 = 8.9$ m, the plasma minor radius $a = 2.9$ m, the on-axis vacuum toroidal field $B_0 = 5.74$ T. The plasma currents in these reference equilibria are I_p=17.75 MA and I_p=19.34 MA, respectively. Note that the target plasma currents are I_p=18 MA and I_p=20 MA, respectively, for these scenarios. We will therefore, where no confusion is caused, also refer to 18 MA and 20 MA scenarios. Matching equilibria with the PT shape (Fig. 1(b)), with the same key parameters as listed above, are also considered. We note that the plasma resistivity differs between the 18 MA and 20 MA equilibria (for both NT and PT) due to the difference in the thermal electron temperature. The corresponding on-axis Lundquist numbers are $S = 5.5\times10^{10}$ for I_p=18 MA and $S = 3.9\times10^{10}$ for I_p=20 MA, for the target plasmas.

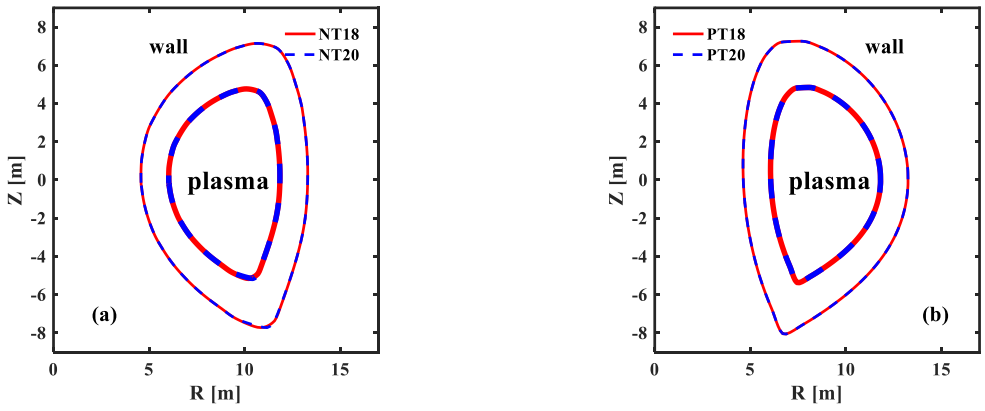

Figure 1. The plasma boundary shapes (thick lines) for the EU DEMO equilibria with (a) negative triangularity (NT) and (b) positive triangularity (PT), plotted together with smoothed shapes of the conformal vacuum vessel (VV) (thin lines). The plasma current is I_p=17.75 MA

in equilibria denoted as “NT18” and “PT18”, and the plasma current is 19.34 MA in equilibria denoted as “NT20” and “PT20”. Note that the plasma boundary shapes nearly overlap for the 18 MA and 20 MA equilibria.

Figure 2 compares radial profiles of the equilibrium quantities for the four plasmas. The safety factors (Fig. 2(a)) are monotonic, with the on-axis value of $q_0 \sim 0.2$ being much lower than that in typical present-day experiments. This low safety factor value is due to the assumption of the presence of the long-period "monster" sawtooth stabilized by a large fraction of energetic particles (in particular fusion-born alphas) in designing the EU DEMO scenarios. A low q_0 value also means that the radial location of the $q = 1$ surface, $r_1 \sim 0.8$, is far away from the magnetic axis and close to the plasma boundary. This fact motivates our investigation of the ideal wall stabilization of the IK mode to be reported in sub-section 3.2.

The surface-averaged toroidal current density profiles (Fig. 2(b)) are similar among four equilibria, explaining the similarity of the safety factor profiles shown in Fig. 2(a). The plasma equilibrium pressure profiles are also similar (Fig. 2(c)). Note the absence of the pressure pedestal in these plasmas. This is because the NT scenario is not expected to be operated in H-mode, due to much reduced favorable magnetic curvature stabilization and hence enhanced ballooning mode instability near the plasma edge. Staying in L-mode of course means generally less energy confinement in a fusion reactor, though recent experiments in DIII-D have demonstrated H-mode like confinement with L-mode plasma with the negative triangularity shape [13], largely due to the fact turbulence at the low-field side (LFS) can be suppressed by large Shafranov shift in the negative triangularity plasma, thanks to strong magnetic field compression at the LFS. On the other hand, no ELMs need to be controlled in a reactor with NT design (in L-mode). The equilibria with positive triangularity (PT), considered in this work, are also in L-mode (i.e. not the baseline design for the EU DEMO which is in H-mode). This is because we wish to have a fair comparison (with the same plasma current and the same L-mode regime) between PT and NT configurations, in terms of the plasma confinement and MHD stability.

A pedestal structure near the plasma edge, produced by the ASTRA code transport simulation [22] with a slight uncertainty at the plasma separatrix, does appear in the density profiles shown in Fig. 2(d). For the IK instability, which is located at the plasma core, this

slight uncertainty near the plasma edge plays a minor role. We also note that the density profiles here are normalized to unity at the magnetic axis.

The equilibrium density and pressure profiles for the fusion-born alpha particles are simulated by the ASCOT code [44] and are shown in Fig. 2(e) and (f), respectively. Note that the alpha density and pressure profiles are normalized by the corresponding thermal electron density and thermal pressure, respectively. For this EU DEMO design, alpha particles contribute about 45% of the thermal fraction to the equilibrium pressure, with about 1.5% of the density fraction. In the following study, in order to ensure the same "fluid" drive for the IK mode, the total equilibrium pressure $P_{eq} = P_{th} + P_{\alpha}$ is kept the same. This means that in the studies where we neglect the alpha particle effects, the portion of the equilibrium pressure associated with P_{α} is effectively replaced by the thermal contribution. The equilibrium distribution for alphas is assumed to be isotropic in particle pitch angle and slowing-down in particle energy [39, 43]. For fusion-born alphas, this type of equilibrium distribution can be analytically calculated by solving the Fokker-Plank equation with simplifying assumptions [45]. The effect of other EPs, e.g., that due to neutral beam injection, is neglected in this study.

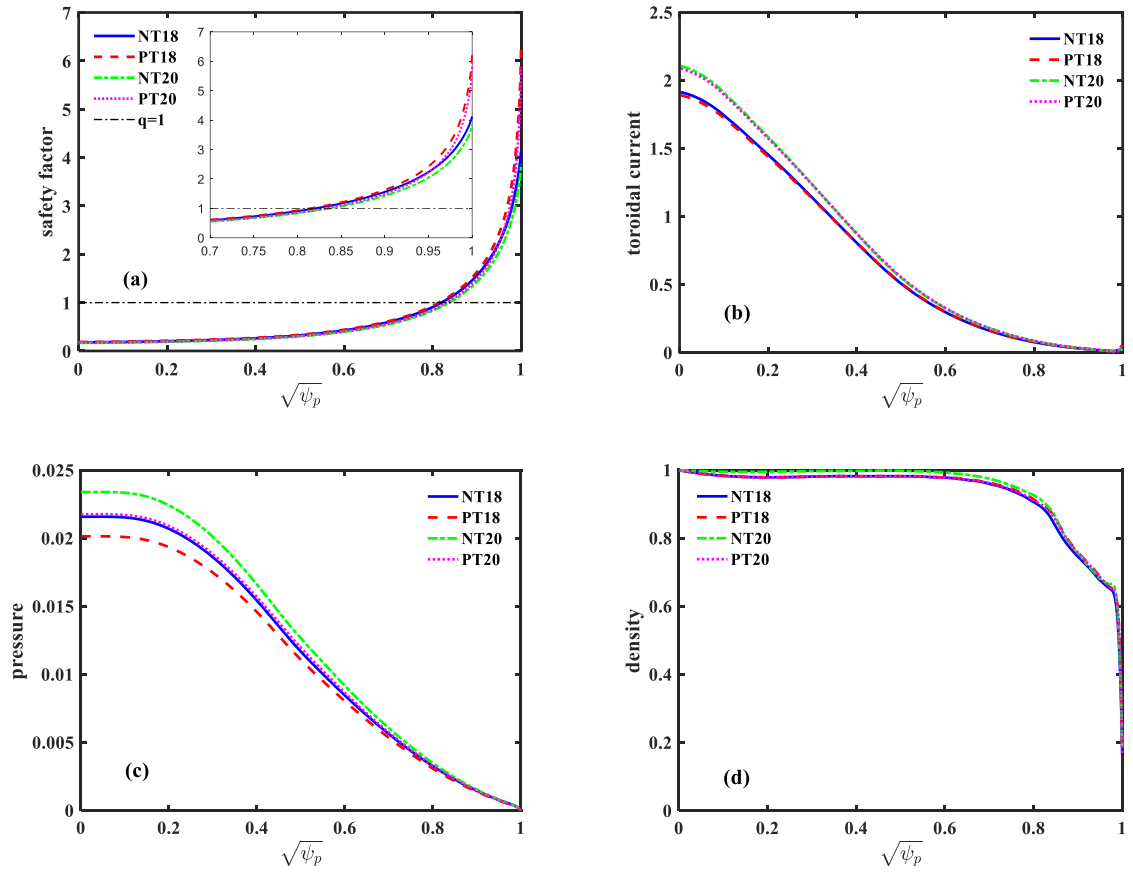

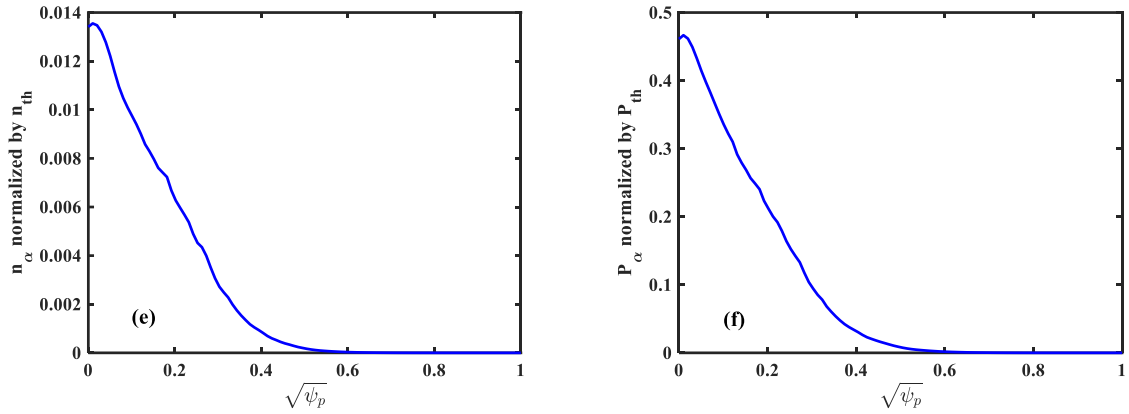

Figure 2. Equilibrium radial profiles for the EU DEMO plasmas, for (*a*) the safety factor q, (*b*) the surface averaged toroidal current density normalized by $R_0 B_0/\mu_0$ (μ_0 being the vacuum magnetic permeability), (*c*) the plasma pressure normalized by B_0^2/μ_0 , (*d*) the density normalized to unity at the magnetic axis, with the plasma current I_p=17.75 MA (solid lines) and 19.34 MA (dashed lines). Equilibrium radial profiles for the (e) density and (f) pressure of fusion-born alpha particles normalized by the corresponding thermal electron density and total thermal pressure, respectively. The horizontal dotted line in plot (*a*) indicates the radial location of the $q = 1$ surface (r_1). Here ψ_p denotes the normalized equilibrium poloidal magnetic flux, and $\sqrt{\psi_p}$ labels the plasma minor radius.

3.2. Effects of ideal wall, plasma resistivity and toroidal flow

Early studies have shown that the ideal IK mode can be stabilized by the presence of an ideally conducting wall [24]. A recent work [23] reports that a close-fitting conducting wall surrounding the plasma can stabilize the ideal IK even when the plasma pressure exceeds the Bussac limit [46]. Recent modelling by the MARS-F code indicates that the effect of the radial location *b*/*a* of the ideal wall on the IK instability is weak for an EU DEMO equilibrium with PT configuration, where the radial location of the $q = 1$ surface ($r_1 = 0.38$) is far away from the plasma edge [30]. On the other hand, a comparative study shows that the ideal-wall beta limit is substantially reduced due to the presence of the internal kink component for a NT plasma [16].

As described in sub-section 3.1, this work considers the EU DEMO equilibria obtained

just before the monster sawtooth crash, characterized by monotonic safety factor profiles with the radial location of the $q=1$ surface (r_1~0.8) being close to the plasma boundary. The role of ideal wall on the mode stability is thus expected to be more pronounced. Note that we assume a perfectly conducting wall here in view of the minor effect of the wall resistivity.

Figure 3 compares the MARS-F computed growth rate γ of the n=1 IK instability for the EU DEMO equilibria with both NT and PT configuration, for both the 18 MA and 20 MA scenarios. All the growth rates and mode frequencies in this work are normalized by the on-axis Alfven frequency $\omega_A = B_0/\left[R_0\left(\mu_0\rho_0\right)\right]$. μ_0 here is the vacuum magnetic permeability and ρ_0 the on-axis plasma density. The mode frequency is not shown in Fig. 3 because it vanishes due to the absence of both plasma equilibrium flow (which we assume here) and drift-kinetic resonance effects. Finite plasma resistivity, with Spitzer model, is assumed here as mentioned before. The IK growth rate significantly increases with the ideal wall being moved away from the plasma boundary. Stabilization however becomes weak as the ideal wall is placed outside the radial location of $b/a>1.5$. When the ideal wall moves sufficiently far from the plasma, the mode growth rate saturates, recovering the value at the no-wall limit. These results suggest that a close-fitting conducting wall plays an important role in the IK stabilization for these EU DEMO plasmas, independent of the NT versus PT configurations.

Furthermore, we observe that the internal kink is more unstable in the NT configuration compared with the PT configuration, for both the 18 MA and 20 MA scenarios. The role of the slightly different pressure (Fig. 2(b)) between the two configurations is negligible. This was confirmed by comparing the mode growth rate with the same normalized plasma pressure β_N. Here, $\beta_N = \beta(\%)a(\mathrm{m})B_0(\mathrm{T})/I_P(\mathrm{MA})$, with $\beta = 2\mu_0\langle p\rangle/B_0^2$ being the ratio of the volume averaged plasma pressure to the magnetic pressure.

Figure 3 also shows that the wall stabilization is more efficient for the 20 MA plasmas, compared to the 18 MA cases. For the 20 MA equilibria, the mode growth rate is reduced by 57% by moving the wall location from $b/a=2$ to the plasma boundary surface ($b/a=1$). The corresponding reduction is 47% for the 18 MA plasmas. Note that similar levels of the growth rate reduction are obtained for the NT and PT configurations.

Figure 4 shows examples of the current patterns on the ideal wall for the NT configuration at I_p=17.75 MA. Selected are four different minor radii: b/a=1.1, 1.3, 1.5 and 2. The wall current pattern changes with the ideal wall moving away from the plasma. In particular, the wall current near the LFS mid-plane weakens relative to that at the HFS, as farther wall distance. We emphasize that the wall current represents part of the eigenfunction of the eigenvalue

problem that we solve here. The overall amplitude of wall current thus has no physics significance and cannot be compared. It is only meaningful to compare the wall current structure.

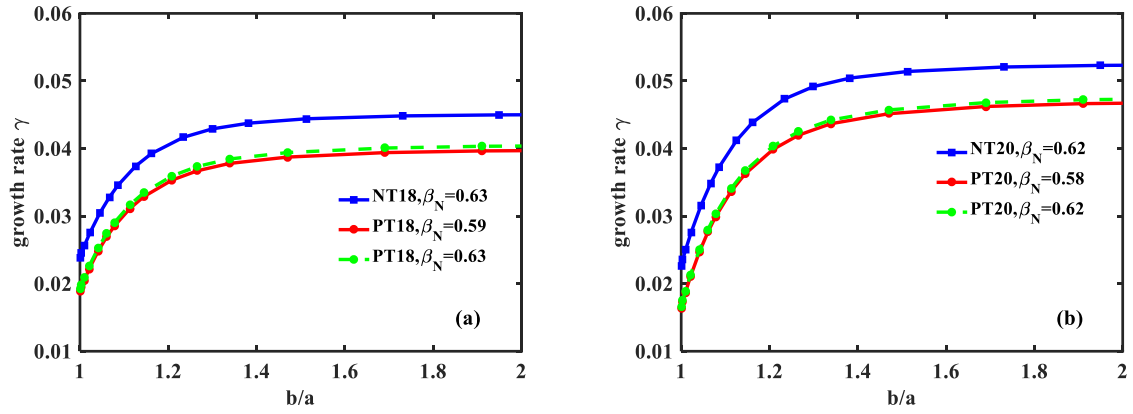

Figure 3. Comparison of the MARS-F computed growth rate γ of the n=1 internal kink instability, normalized by the on-axis Alfven frequency $\omega_A = B_0/\left[R_0\left(\mu_0\rho_0\right)\right]$, for equilibria with NT and PT configurations, and with the plasma current of (*a*) I_p=17.75 MA and (*b*) I_p= 19.34 MA. The growth rate is given as a function of the radial location *b/a* of the ideal conducting wall. β_N is normalized plasma pressure. The plasma resistivity is calculated using the Spitzer model, so the on-axis Lundquist number $S = 5.5\times10^{10}$ for I_p=18 MA and S=3.9×10^{10} for I_p=20 MA due to the different electron temperatures T_e for two cases.

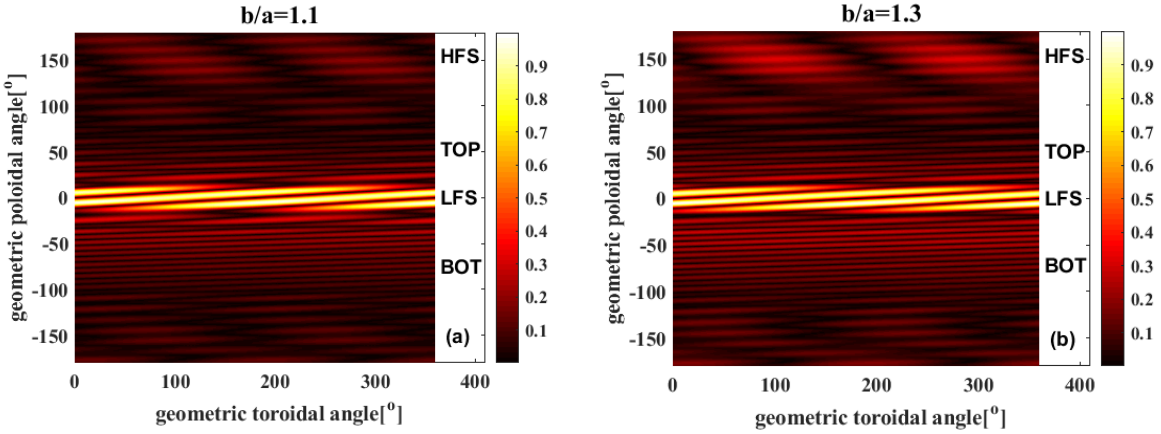

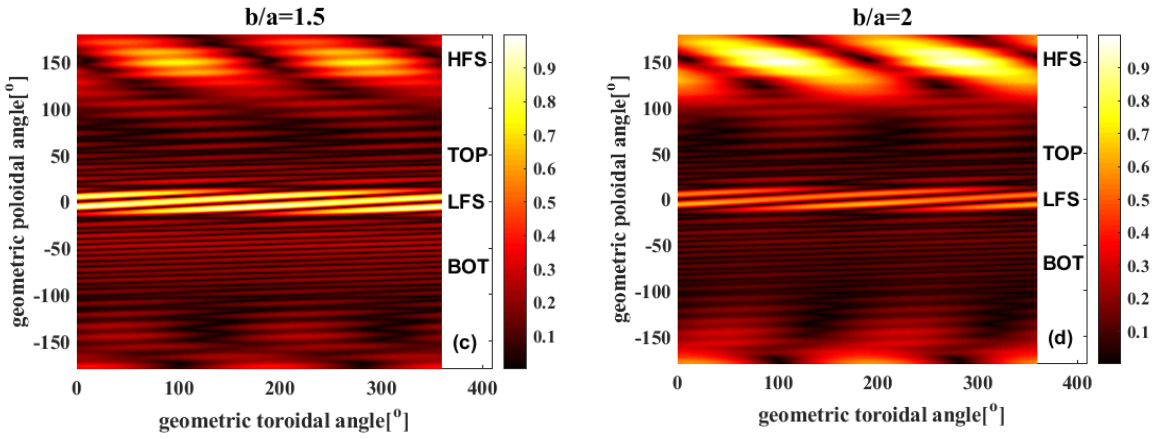

Figure 4. Computed current patterns on the ideal wall for the NT configuration at I_p=17.75 MA, with the wall located at four different minor radii (*a*) *b/a*=1.1, (*b*) *b/a*=1.3, (*c*) *b/a*=1.5, and (*d*) *b/a*=2.

Next, we consider the effect of the plasma resistivity on the IK instability, while still assuming the fluid model (MARS-F) with vanishing equilibrium flow. The results, reported in Fig. 5, shows that the plasma resistivity destabilizes the IK – a result which is well known for the PT configuration [23, 30] and is now found to be valid also for the NT configuration. The synergistic stabilization effects due to the plasma conductivity and the ideal wall (with infinite conductivity) result in the least unstable IK towards the lower-right corner of the 2D parameter space shown in Fig. 5, i.e. by assuming a perfectly conducting wall located at the plasma boundary surface and an ideal plasma condition. Note that these stabilization trends hold for both the NT and PT plasmas in EU DEMO. The only quantitative difference is that the NT equilibria are slightly more unstable than the PT counterparts.

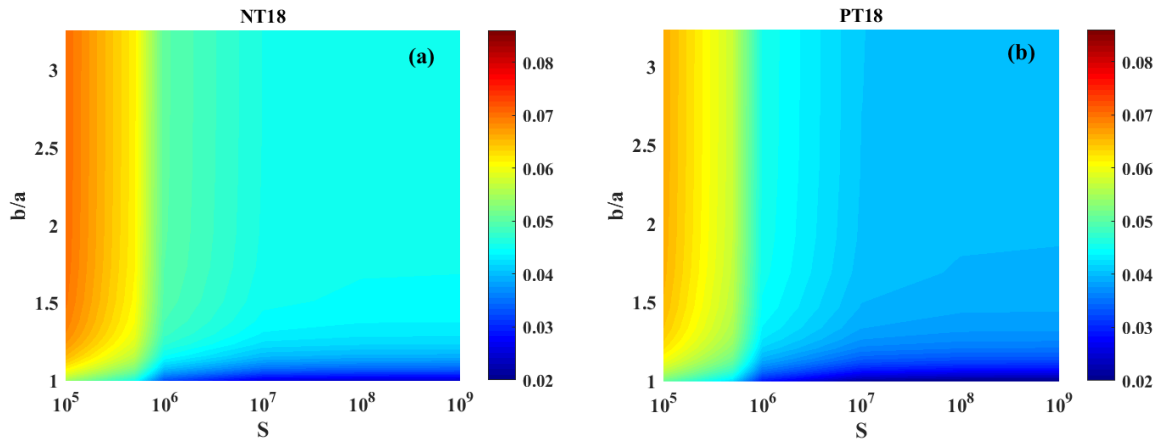

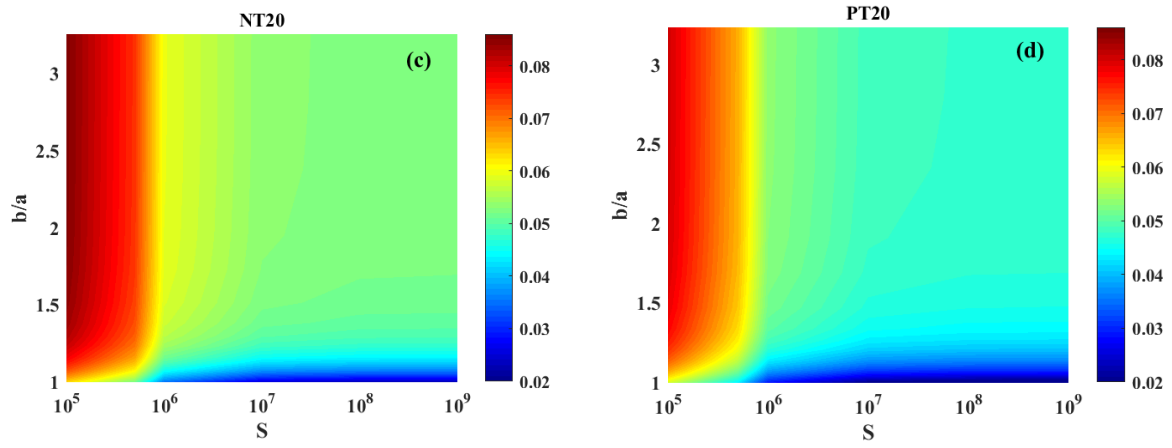

Figure 5. Comparison of the MARS-F computed growth rate of the $n = 1$ resistive internal kink instability, normalized by the on-axis Alfven frequency ω_A, with varying Lundquist number S (horizontal axis) and the radial location b/a of the ideal conducting wall (vertical axis). Four cases are included: (*a*) the plasma current I_p=17.75 MA and NT (NT18), (*b*) the plasma current I_p=17.75 MA and PT (PT18), (*c*) the plasma current I_p=19.34 MA and NT (NT20), and (*d*) the plasma current I_p=19.34 MA and PT (PT20), respectively. Zero plasma flow is assumed (Ω=0).

Next, we study the effect of plasma toroidal flow on the IK instability in these EU DEMO plasmas. Plasma flow is known to play an important role in the IK instability in tokamak plasmas. It has been analytically established that the IK mode is stabilized by toroidal rotation at angular frequency of order $\Omega/\omega_A \sim \varepsilon$, with $\varepsilon = 1/A$ being the inverse aspect ratio [47]. Nonlinear simulations found that toroidal flow can significantly influence the nonlinear dynamics of the non-resonant IK mode [48]. For the EU DEMO design, plasma flow is expected to be relatively slow. Therefore, we shall limit our study in the subsonic flow regime. In this regime, the flow-induced modification to the plasma equilibrium can be neglected, because the modification is proportional to the sound Mach number squared. Although previous modeling for a simple equilibrium has demonstrated relatively weak effect of subsonic toroidal flow on the IK stability [26], the effect remains to be quantified for EU DEMO plasmas with strong shaping.

One uncertainty with the DEMO plasma design is the precise radial shape of the toroidal rotation profile. For simplicity, we shall assume a fixed radial profile modeled for an ITER 15 MA baseline scenario, as reported in Fig. 18(b) from Ref. [49]. The same profile, which

monotonically decreases with the plasma radial coordinate, will be used for all four equilibria studied here. The overall amplitude, i.e., the on-axis rotation frequencies Ω/ω_A, is scanned from 0 to 5×10^{-2}, with the stability results reported in Fig. 6. Note that we assume ideal plasma here (η=0) while considering two extreme locations of the ideal wall: b/a=1 and 2, respectively.

Figure 6 shows that, within the subsonic flow assumption, toroidal rotation has weak effect on the IK instability in EU DEMO, for both NT and PT configurations. This holds independent of the plasma current (17.75 MA versus 19.34 MA). With a close-fitting ideal wall (b/a=1, Fig. 6(a)), a slight destabilization of the mode is computed at sufficiently fast flow ($\Omega/\omega_A>10^{-2}$), most likely due to the flow shear destabilization, i.e., the Kelvin-Helmholtz mechanism [50]. This trend is reversed for cases with far wall (b/a=2, Fig. 6(c)), probably due to the gyroscopic stabilization mechanism [51]. The mode frequency is roughly proportional to the on-axis rotation frequency (Fig. 6(b,d)), as expected for internal kink.

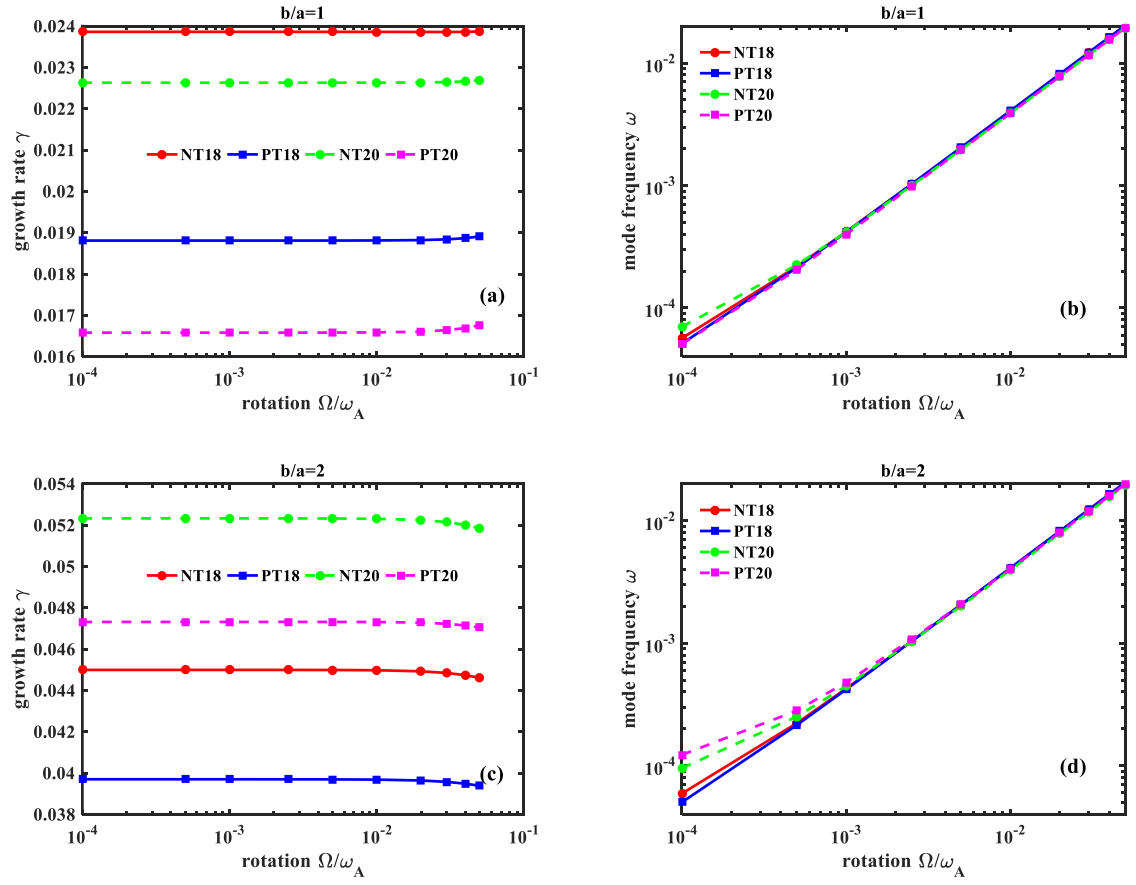

Figure 6. The growth rate γ (left pannel) and mode frequency ω (right pannel) of the n=1

internal kink instability with varying plasma on-axis rotation frequency, for four equilibria: (i) NT18, (ii) PT18 , (iii) NT20, and (iv) PT20, respectively. Both the eigenvalue (γ , ω) and the rotation are normalized by the on-axis Alfven frequency ω_A. An ideal wall is placed (*a, b*) at the plasma boundary: *b/a* = 1 or (*c, d*) far away from the plasma surface: *b*/*a* = 2. Ideal plasma is assumed (η=0).

3.3 Drift-kinetic effects on internal kink stability

As the major part of the present study, we now investigate drift-kinetic effects on the IK stability in both NT and PT EU DEMO plasmas, following both perturbative and non-perturbative approaches. In the perturbative approach, the perturbed drift-kinetic energy is evaluated with the eigenfunction computed for an ideal fluid IK mode, while the non-perturbative MARS-K formulation allows self-consistent modification of the mode eigenfunction and eigenvalue by drift-kinetic effects. Furthermore, the non-perturbative MHD-kinetic hybrid formulation directly computes the mode eigenvalue, which will be compared with that obtained from the perturbative approach based on the perturbed energy principle for IK.

3.3.1 Kinetic effects following perturbative approach

The perturbative approach employs the extended energy principle for the IK mode [25]

$$-\delta\hat{W} = -\left(\delta\hat{W}_f + \delta\hat{W}_{th} + \delta\hat{W}_\alpha\right) = \gamma \qquad (9)$$

where $\delta\hat{W}_f$, $\delta\hat{W}_{th}$ and $\delta\hat{W}_\alpha$ represent the perturbed potential energies from the fluid contribution (computed by MARS-F), the drift-kinetic components of thermal and alpha particles (computed by MARS-K), respectively. These energy components are normalized by the product of a constant (as shown in Fig. 7) and the inertial term δI associated with the radial displacement of the plasma (see below). $\delta\hat{W}$ is the normalized total perturbed potential energy, representing the mode eigenvalue γ normalized by the on-axis Alfven frequency ω_A.

We emphasize that Eq. (9) is valid when the layer physics effects around the $q=1$ surface are not important, i.e., when the following condition is satisfied [25]

$$-\delta\hat{W} > -\delta\hat{W}_c = \max\left\{\hat{\rho}, \omega_*^{thi}\tau_A/2\right\} \quad (10)$$

where $\hat{\rho} = \rho_i/\overline{r}_1$, with ρ_i being the thermal ion Larmor radius and $\overline{r}_1$ the averaged radius of the q=1 surfac. ω_*^{thi} denotes the thermal ion diamagnetic frequency and τ_A the Alfven time. For the EU DEMO plasmas considered in this work, we estimate the critical value $-\delta\hat{W}_c \sim 2.6\times10^{-3}$ for the I_p=17.75 MA equilibrium and $-\delta\hat{W}_c \sim 3.5\times10^{-3}$ for the I_p=19.34 MA equilibrium. Details in evaluating these estimates are presented in Appendix A.

The perturbed fluid potential energy δW_f and the plasma inertia δI are computed by MARS-F while scanning the ideal wall radius, resulting in fluid IK with varying growth rate $\gamma = \gamma_f$. The ratio of the potential to inertial energies versus the mode growth rate is plotted in Fig. 7, for four plasma equilibria. By applying a linear fitting

$$-\frac{\delta W_f}{\delta I} = c_1\gamma_f + c_2 \quad (11)$$

we obtain the values for coefficients c_1 and c_2 which do not depend on the wall location but are generally different for different plasma equilibria. We find $c_2/c_1 \sim O(10^{-3})$ for these EU DEMO plasmas (Fig. 7). Therefore, Eq. (11) can be approximately expressed as

$$\gamma_f \approx -\frac{\delta W_f}{c_1\delta I} \equiv -\delta\hat{W}_f \quad (12)$$

which has the same form as Eq. (9). Since $-\delta\hat{W}_f \approx \gamma_f \sim O(10^{-2})$ and $-\delta\hat{W}_c \sim O(10^{-3})$, the condition $-\delta\hat{W}_f > -\delta\hat{W}_c$ holds well for all four equilibria, indicating that the IK instability in these EU DEMO plasmas are mainly determined by the perturbed potential energy and much less by the layer physics. Note that the normalization constant c_1 from Eq. (12) is important, since this allows us to calculate the IK growth rate when drift-kinetic effects from thermal and alpha particles are included into the perturbative analysis. The values of c_1 are shown in Fig. 7. Note that c_1 is about 25% larger for the NT configuration than the corresponding PT configuration with the same plasma current.

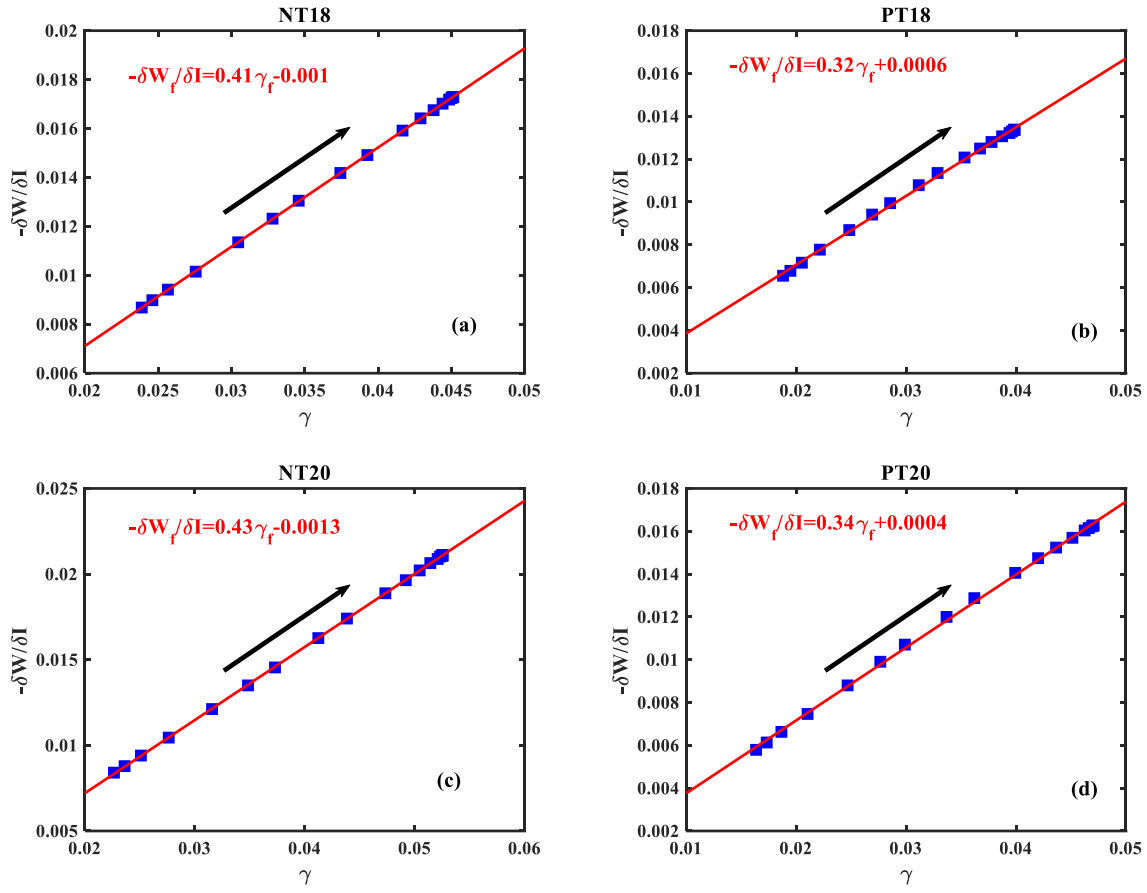

Figure 7. The MARS-F computed perturbed fluid potential energy $-\delta W_f$ (with negative sign), normalized by the plasma inertia δI associated with the radial displacement (blue dots), versus the growth rate γ, normalized by the on-axis Alfven frequency ω_A, at fixed S=5.5×10^{10} for the I_p=17.75 MA cases and S=3.9×10^{10} for the I_p=19.34 MA cases. Four cases are included: (*a*) NT18, (*b*) PT18, (*c*) NT20, and (*d*) PT20, respectively. Analytic fittings of the normalized potential energy $-\delta W_f / \delta I$ (red lines) are also presented in the figures. The variations of γ and $-\delta W_f / \delta I$ occur as the ideal wall location moves from *b*/*a*=1 to *b*/*a*=3. The direction of the black arrow indicates increasing distance between the ideal wall and the plasma boundary. Vanishing plasma flow is assumed (Ω=0).

Next, we compute the perturbed drift-kinetic energies associated with thermal and alpha particles, using the fluid IK eigenfunction. Figure 8 reports the real part of various drift-kinetic energy non-adiabatic components associated with the toroidal drift precession of trapped thermal ions (i-NTD), electrons (e-NTD) or trapped fusion-born alphas (α-NTD), the bounce

motion of trapped thermal ions (i-NTB) as well as the transit motion of passing thermal ions (i-NP), while scanning the ideal wall radius. Note that other drift-kinetic contributions, e.g., that due to bounce or transit motion of thermal electrons or alpha particles, are deemed small and are thus neglected in this study. For these equilibria, the imaginary part of the perturbed drift-kinetic energy is always about two orders of magnitude smaller than the real part, and is thus neglected in further analysis.

The key observations from Fig. 8 are the following. (i) All the drift-kinetic potential energies (δW_k) are of positive values, indicating stabilizing effect on the IK mode. (ii) The strongest stabilization effect comes from passing thermal ions (i-NP), whilst the precessional drift resonance of trapped alpha particles (α-NTD) provides the weakest effect. (iii) As the distance between the ideal wall and the plasma boundary increases within the range of b/a = 1-1.3, the drift-kinetic contributions generally decrease. The exception is the contribution from passing thermal ions (i-NP), which stays nearly a constant. (iv) Apart from the amplitude of kinetic energy components, there is no qualitative difference between the NT and PT plasmas.

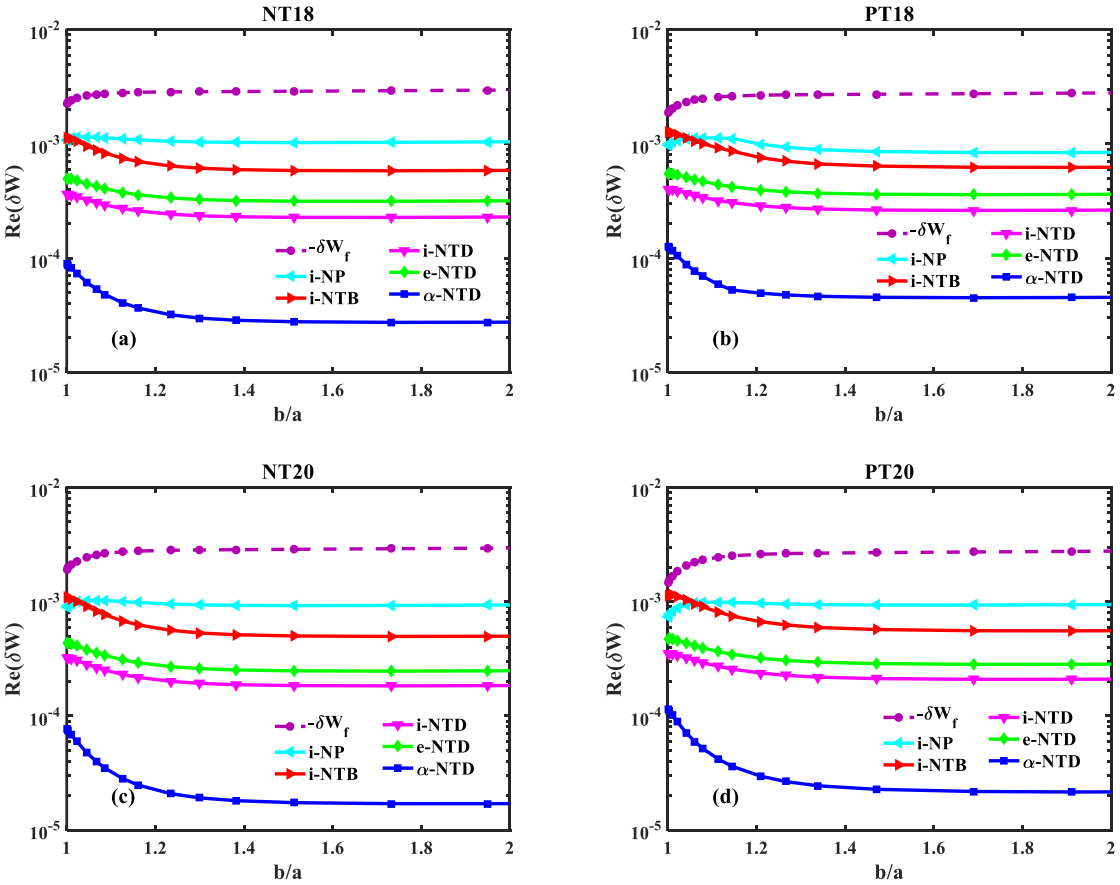

Figure 8. The energy perturbations versus the location b/a of the ideal wall for (*a*) NT18, (*b*) PT18 , (*c*) NT20, and (*d*) PT20, respectively. Plotted is the *opposite number* of fluid potential energy ($-\delta W_f$), together with the perturbatively computed kinetic energy of the internal kink mode from the non-adiabatic contribution of the transit resonance of passing thermal ions (i-NP), the bounce motion of trapped thermal ions (i-NTB), the toroidal precession of trapped thermal ions (i-NTD), electrons (e-NTD) or trapped fusion-born alpha particles (α-NTD). Other parameters are $S=5.5\times10^{10}$ for the I_p=17.75 MA cases and $S=3.9\times10^{10}$ for the I_p=19.34 MA cases, Ω=0.

The fluid and drift-kinetic energy perturbations shown in Fig. 8 are used to estimate growth rates of the IK mode with partial or full inclusion of kinetic effects following the perturbative approach

$$\gamma_{kj} = -\left(\delta\hat{W}_f + \delta\hat{W}_{kj}\right) \equiv -\frac{\delta W_f + \delta W_{kj}}{c_1 \delta I} \tag{13}$$

where j signifies the species of the kinetic effects from various particles. Note that Eq. (13) comes from Eq. (9) and Eq. (12), where c_1, $\delta\hat{W}_f$ and δI are evidently invariant quantities for a given plasma equilibrium.

The mode growth rate, with various combinations of drift-kinetic effects, is reported in Fig. 9, again scanning the ideal wall radius. The most significant result here is that the perturbative analysis predicts full kinetic stabilization of the IK mode, when the ideal wall is placed sufficiently close to the plasma boundary. This robustly holds (for all four scenarios) when all the thermal contributions are included. Compared with the PT configuration, a narrower stable window is predicted for the NT configuration. As a qualitative difference, complete stabilization of the mode still occurs in the PT plasma, but not in the NT plasma, when we leave out the kinetic contribution from passing thermal ions (i-NP). Furthermore, the stabilizing effect from the toroidal precession of trapped thermal particles (ions and electrons) is comparable to that from bounce motion of trapped thermal ions. The stabilizing effect of trapped alpha particles is very small in all four EU DEMO plasmas. In general, the fluid/kinetic growth rate for the NT configuration is larger than that for PT, with similar equilibrium profiles. In terms of the perturbed fluid and kinetic potential energies, this is related to (i) the normalized

fluid energy satisfying $-\delta\hat{W}_f(\mathrm{NT}) > -\delta\hat{W}_f(\mathrm{PT})$ and (ii) the normalized kinetic energy satisfying $\delta\hat{W}_{kj}(\mathrm{NT}) < \delta\hat{W}_{kj}(\mathrm{PT})$ (except for the i-NP case) . In other words, the combined effect of stronger fluid drive and weaker kinetic damping explains why the NT configuration is more unstable than the PT counterpart.

We point out that the layer physics around $q=1$ become important as the mode growth rate reduces to the critical value $-\delta\hat{W}_c$, indicated by the horizontal dashed lines in Fig. 9. The layer physics is still negligible when the precessional drift effect alone is considered. This means that caution need to be taken when the IK stability approaches the marginal point following the perturbative analysis, due to the lack of the layer contribution.

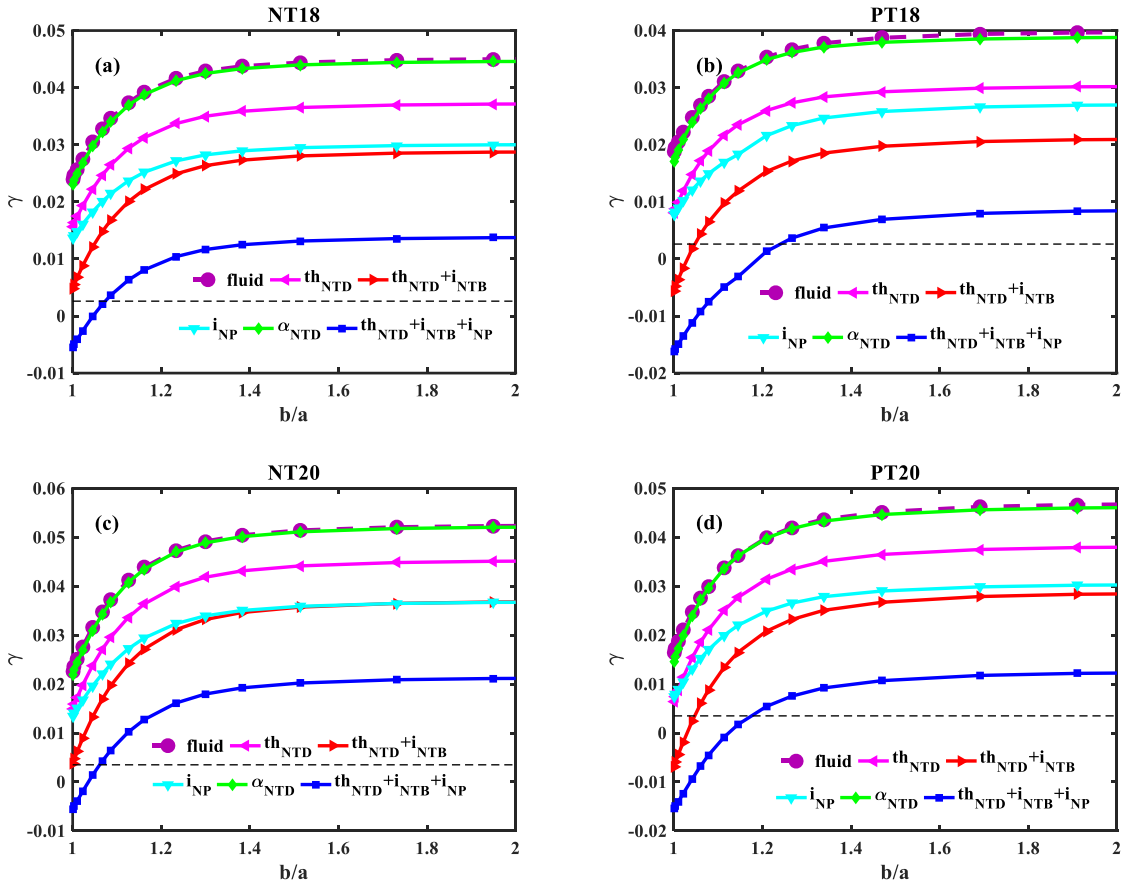

Figure 9. The growth rate γ of the *n*=1 internal kink mode, normalized by the on-axis Alfven frequency ω_A, versus the location *b*/*a* of the ideal wall for (*a*) NT18, (*b*) PT18 , (*c*) NT20, and (*d*) PT20, respectively. Plotted is the fluid growth rate computed by MARS-F ('fluid'), together with the various kinetic growth rates of the internal kink mode due to the non-adiabatic

contribution from transit resonance of passing thermal ions (i-NP), the bounce motion of trapped thermal ions (i-NTB), as well as the toroidal precession of trapped thermal ions (i-NTD), electrons (e-NTD) or trapped fusion-born alpha particles (α-NTD) following the perturbative approach. Other parameters are $S=5.5\times10^{10}$ for the I_p=17.75 MA case and $S=3.9\times10^{10}$ for the I_p=19.34 MA case, Ω=0 for all cases. The kinetic growth rates are evaluated using Eq. 13.

3.3.2 Kinetic effects following non-perturbative approach and comparison with perturbative results

In what follows, we compute the IK stability based on the self-consistent MHD-kinetic hybrid model within MARS-K. Figures 10-11 compare the mode growth rate between the self-consistent ("SC") and the perturbative ("P") models, assuming two radial locations for the ideal wall, $b/a=1$ (Fig. 10) and $b/a=2$ (Fig. 11), respectively. In each plot, we consider several combinations of drift-kinetic contributions: the toroidal precession of trapped thermal particles alone (th_{NTD}), addition of bounce resonance contributions (th_{NTD}+i_{NTB}), non-adiabatic contribution from transit motion of passing thermal ions (i_{NP}), and finally the toroidal precession of trapped fusion-born alphas (α_{NTD}).

In the following, we compare results predicted by the self-consistent and perturbative approaches for the NT and PT plasmas. The common observation is that trapped fusion-born alphas provides minor stabilization to the IK mode. This is due to two factors. (i) The mode considered here is strongly unstable, leading to a large imaginary part in the denominator of Eq. (8), which in turn reduces the resonance effect between the mode and plasma particles. (ii) This kinetic resonance contribution is further reduced for alphas, because the latter are predominantly located in the plasma core region within r<0.4 (Fig. 2(c-d)), whereas the radial displacement associated with the IK extends to the r~0.8 surface. The drift kinetic energy perturbation is proportional to $|\xi_\perp|^2$, with the latter being the plasma displacement perpendicular to the equilibrium magnetic field lines and consisting of both radial and poloidal components. The poloidal displacement associated with the IK is largely localized near the q=1 surface, where the fusion born alphas are almost absent. Therefore, the strong IK instability

occurs due to the low q_0 value for the equilibria studied in this work. Energetic particles should have stronger stabilization effect on weakly unstable and more core-localized IK (occurring as q_0 is close to 1), which in turn can lead to monster sawteeth.

With inclusion of the toroidal precession of trapped thermal particles (ions and electrons) and the bounce motion of trapped thermal ions, both approaches predict (partial) stabilization of the mode, but quantitatively differ in the computed mode growth rate. The self-consistent approach generally predicts weak stabilization of the mode in all cases. But much stronger stabilization is obtained with the perturbative approach. In particular, the perturbative analysis shows strong stabilization due to the bounce motion of trapped thermal ions, which is less pronounced with the self-consistent computations. We remark that physics-wise, the self-consistent approach differs from the perturbative approach in two aspects: (i) the former allows kinetic modification of the eigenmode structure; (ii) the mode eigenvalue is self-consistently (and non-linearly) included in evaluating the drift-kinetic integrals in the non-perturbative treatment [32]. Finally, we mention that the quantitative differences between the perturbative and non-perturbative predictions are independent of the NT versus PT plasma boundary shapes.

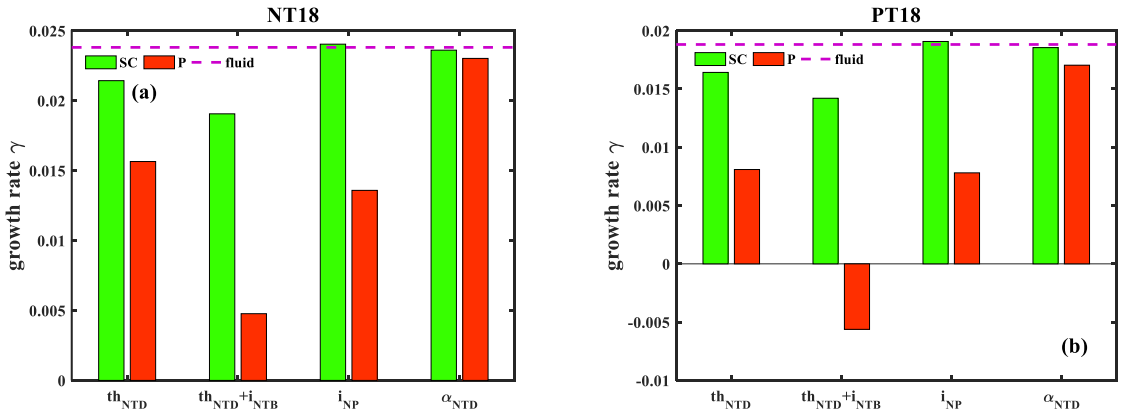

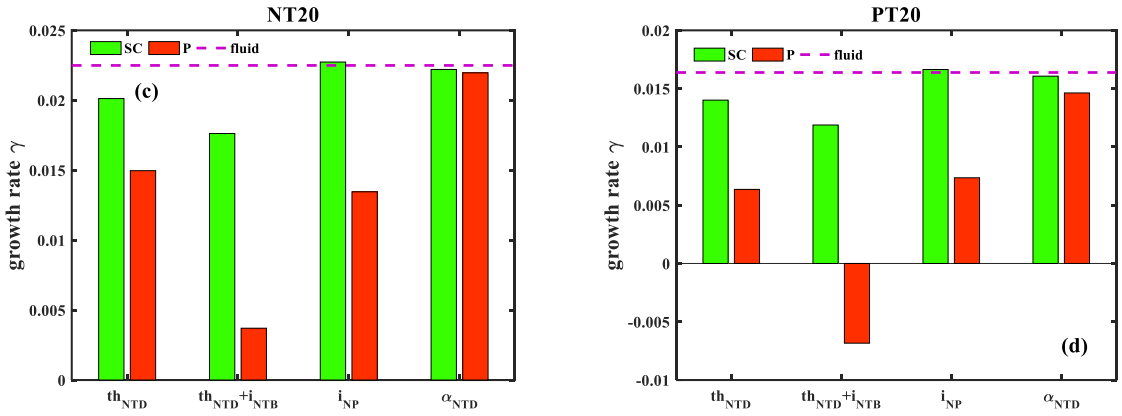

Figure 10. The MARS-K computed growth rate γ of the n = 1 internal kink, normalized by the on-axis Alfven frequency ω_A, with each group representing inclusion of a specific drift-kinetic effect—the toroidal precession of trapped thermal particle with or without the bounce motion of trapped thermal ions (th_{NTD} or th_{NTD}+i_{NTB}), the non-adiabatic contribution from transit resonance of passing thermal ions (i_{NP}) as well as the toroidal precession of trapped fusion-born alpha particles (α_{NTD}). Within each group, comparison is also made between the self-consistent approach and the perturbative approach. Four cases are included: (*a*) NT18, (*b*) PT18 , (*c*) NT20, and (*d*) PT20, respectively. An ideal wall is placed at the plasma boundary: $b/a=1$. Other parameters are S=5.5×10^{10} for the I_p=17.75 MA cases and S=3.9×10^{10} for the I_p=19.34 MA cases. Ω=0 for all cases. The horizontal dashed lines indicate the fluid growth rate of the n = 1 internal kink, computed by MARS-F and normalized by the on-axis Alfven frequency.

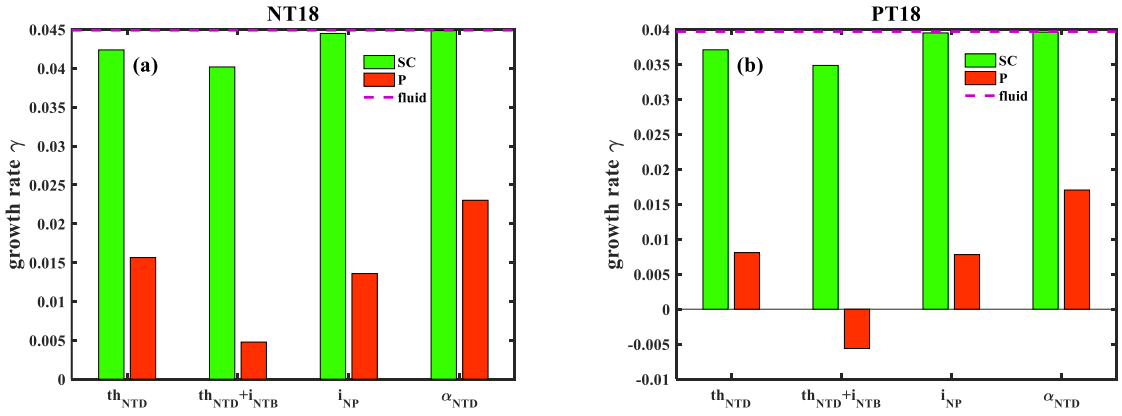

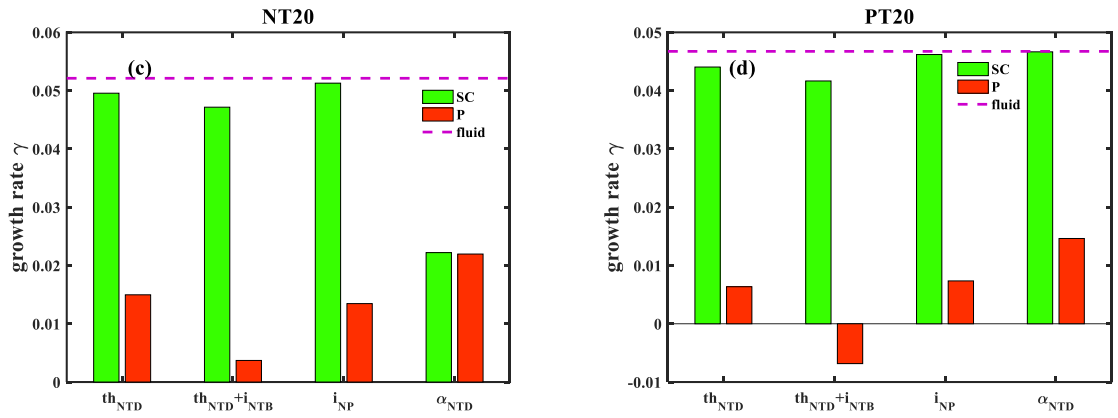

Figure 11. The MARS-K computed growth rate γ of the n = 1 internal kink, normalized by the on-axis Alfven frequency. An ideal wall is placed far away from the plasma surface, radius, at $b/a = 2$. Other parameters are same as Fig. 10.

The eigenmode structures between the perturbative and non-perturbative analysis, as well as that between the NT and PT shapes, are compared in Fig. 12 for the I_p=17.75 MA plasmas. The poloidal Fourier harmonics of the computed plasma radial displacement (Fig. 12(a-b)) are similar between the fluid IK mode employed in the perturbative analysis, and the kinetic IK obtained with the self-consistent hybrid model. Although not shown here, similar observations are also made for the I_p=19.34 MA plasmas. This indicates that the difference in the mode stability, between the perturbative and non-perturbative calculations, is primarily due to the self-consistent determination of the mode eigenvalue in the latter. We note that a similar conclusion was achieved in studying the resistive wall mode stability for an ITER plasma [38]. Finally, we again point out that the overall amplitude of the eigenfunction shown here has no physics significance. It is therefore only meaningful to compare the overall structure of the plasma displacement.

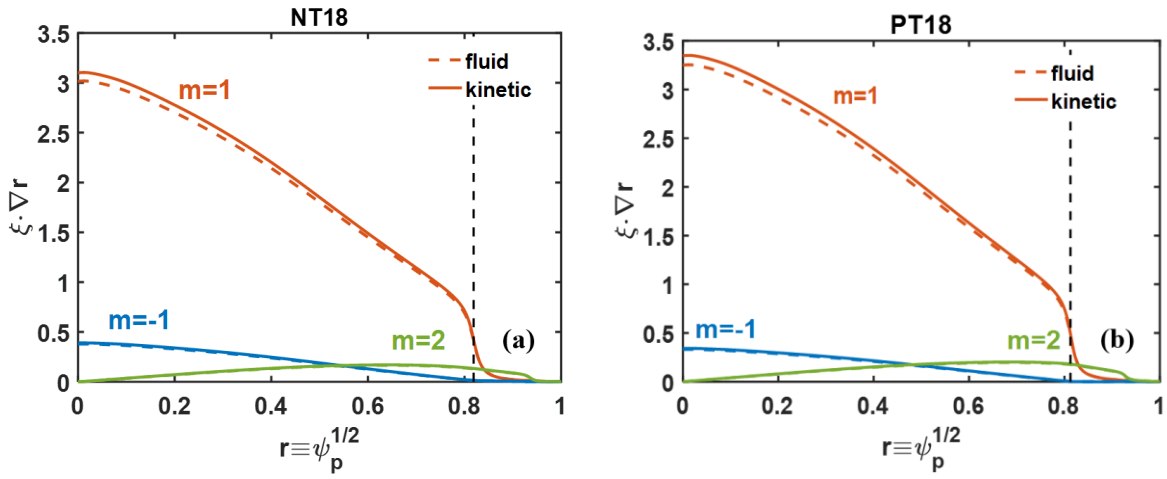

Figure 12. Comparison of the poloidal Fourier harmonics of the eigenfunction (the radial displacement) between the fluid and the kinetic n=1 internal kink mode, with (a) NT and (b) PT. Only the toroidal precession of trapped thermal particle and the bounce motion of trapped thermal ions (th_{NTD}+i_{NTB}) is included for kinetic eigenfunction. An ideal conducting wall is placed far away from the plasma surface, radius, at $b/a = 2$. Other parameters are S=5.5×10^{10}, I_p=17.75 MA, and Ω=0.

Next, the similarity in the IK mode stability between the NT and PT shapes is also reflected in the similarity of the mode eigenfunctions as shown in Fig. 13. In particular, Fig. 13 shows examples of the 2D mode structure in the poloidal plane, with inclusion of drift-kinetic contributions from thermal particles. It is evident that the region occupied by the IK instability has a close-to-circular shape, which is not much affected by the plasma triangularity. This is likely the reason that the plasma shaping has limited influence on the IK instability in these EU DEMO plasmas.

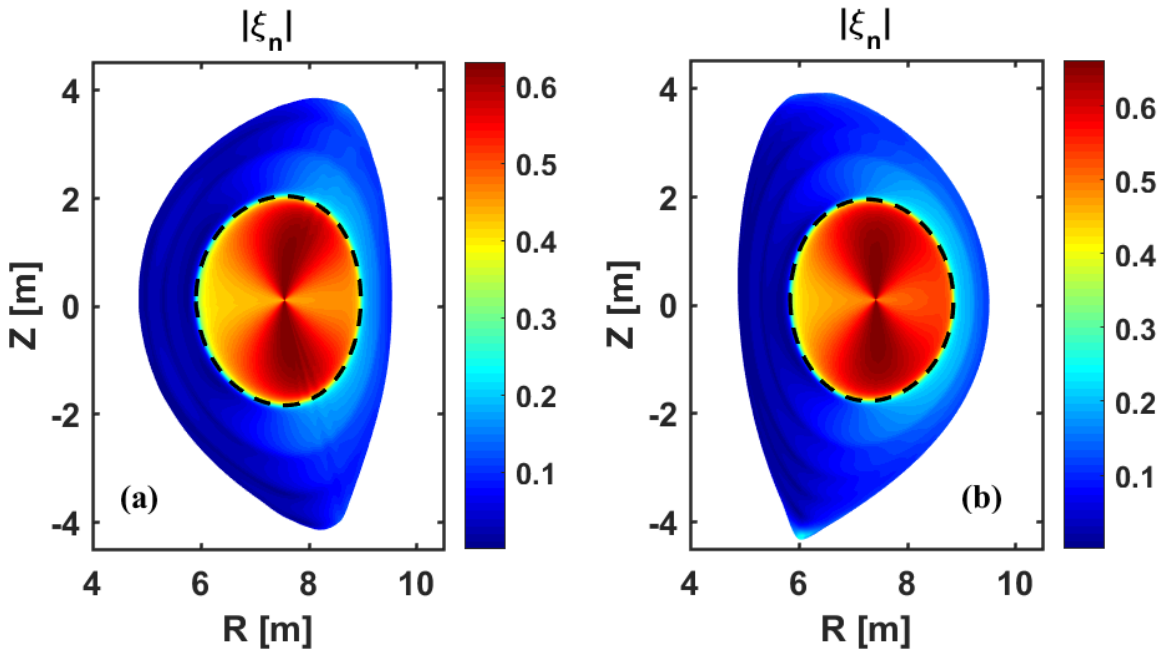

Figure 13. Comparison of the kinetic n = 1 internal kink eigenfunctions, including components from the toroidal precession of trapped thermal particle and the bounce motion of trapped thermal ions (th_{NTD}+i_{NTB}), in terms of amplitude of the plasma radial displacement, for (a) the case with NT and (b) the case with PT in 2D plane. An ideal conducting wall is placed far away from the plasma surface, radius, at $b/a = 2$. Other parameters are S=5.5×10^{10}, I_p=17.75 MA, and Ω=0. The black dashed line represents the q=1 surface.

4. Summary

We have carried out the numerical study of the internal kink stability for the EU DEMO scenarios with both negative and positive triangularity shapes. The designed plasma equilibria, at I_p=17.75 MA and 19.34 MA plasma currents, are reconstructed right before the monster sawtooth (due to fusion- born alpha stabilization) and thus have low values of the on-axis safety factor (q_0~0.2) and large radius (r_1~0.8) for the $q = 1$ surface. Various important factors, including the radial location of the conducting wall, the plasma resistivity and toroidal flow, the drift-kinetic effects from thermal and alpha particles, are all investigated for the IK stability of these equilibria.

For the NT plasmas, the IK becomes more unstable as an ideal conformal wall moves away from the plasma boundary, with the mode growth rate saturates at the wall radial location

of about $b/a = 1.5$. The plasma resistivity destabilizes the IK mode. The effect of sub-sonic toroidal plasma flow is sufficiently weak and can thus be ignored for these EU DEMO equilibria. These results are consistent with that of PT plasmas, albeit the mode is more unstable in the NT plasmas than in the PT counterparts.

Both perturbative and self-consistent drift-kinetic calculations predict (partial) stabilization of the IK modes in both NT and PT configurations, with inclusion of various kinetic contributions. Precessional drift motion of trapped fusion-born alphas in EU DEMO produces weak stabilization to the IK mode. Stronger stabilization occurs with the toroidal precession of trapped thermal particles (ions and electrons) and the bounce-transit motion of thermal ions. The stabilization is similar between the NT and PT configurations, due to the similarity of the mode eigenfunction (occupying a nearly circular region in the plasma core) despite the sign difference in the triangularity. The non-perturbative MHD-kinetic hybrid model predicts much less stabilization of the mode than the perturbative model, primarily due to the self-consistent determination of the mode eigenvalue in the former. The non-perturbative results, representing more conservative estimate on the IK instability in EU DEMO, are physically more accurate.

The fact that the IK is found to be more unstable in the NT plasma than that in the PT plasma in EU DEMO, with the same equilibrium profiles, suggests that more frequent sawteeth may occur with NT, which is generally good in terms of flushing away core impurities and reducing energy release per sawtooth. On the other hand, since the enhancement of the IK instability by NT is not substantial as we found in this study, we do not expect a dramatic effect that NT can bring to a future reactor, as long as IK and sawteeth are concerned, compared to the PT configuration. Experiments and modeling efforts (with MARS-K) on IK/sawteeth behavior are currently on-going in present day tokamaks.

We remark that subtle physics effects, such as the resistive layer physics and the finite Larmor radius stabilization for the IK, are neglected in this study. This is justified by the fact that the mode is predicted to be strongly unstable and far from the marginal stability in these EU DEMO plasmas (in particular with the non-perturbative hybrid model). For the fusion-born alphas, the finite orbit-width effect is also neglected in the drift-kinetic computations. As shown in Ref. [52], the first-order finite orbit-width correction to the precessional drift resonances of trapped energetic particles vanishes. Finally, this study ignores kinetic effects from other

energetic particles, such as that due to neutral beam injection.

Acknowledgments

We thank Drs Hartmut Zohm, Maviglia Francesco, Justin Ball, Li Li, Guoliang Xia, Jing Ren, Shuo Wang, Xu Yang, Neng Zhang and Yutian Miao for useful discussions and help. This work is supported by "the Fundamental Research Funds for the Central Universities" (grant number 3132020181). The work is also supported by the U.S. DoE Office of Science under Contract Nos. DE-FG02–95ER54309 and DE-FC02–04ER54698.

Appendix A. Estimates of the $-\delta\hat{W}_c$ values for EU DEMO equilibria

In this appendix, we estimate the $-\delta\hat{W}_c$ values for EU DEMO for the $I_\mathrm{p}=18$ MA and $I_\mathrm{p}=20$ MA scenarios, following a similar procedure applied to ITER [25]. The D-T plasma is assumed, i.e., the average ion-to-proton mass ratio is assumed $\mu=2.5$. The ion temperature is $T_i=20$ keV for the $I_\mathrm{p}=18$ MA scenario and $T_i=25.3$ keV for the $I_\mathrm{p}=20$ MA scenario. Thermal ion velocity $v_{thi}=\sqrt{T_{thi}/m_{thi}}$ can thus be assessed

$$v_{thi}(18\ \mathrm{MA})=\sqrt{\frac{T_i^{18}}{\mu m_p}}=\sqrt{\frac{20\times10^3\ \mathrm{eV}\times1.6022\times10^{-19}\ \mathrm{J/C}}{2.5\times1.67261\times10^{-27}\ \mathrm{kg}}}=0.8754\times10^6\ \mathrm{m/s} \tag{A.1}$$

$$v_{thi}(20\ \mathrm{MA})=\sqrt{\frac{T_i^{20}}{\mu m_p}}=\sqrt{\frac{25.3\times10^3\ \mathrm{eV}\times1.6022\times10^{-19}\ \mathrm{J/C}}{2.5\times1.67261\times10^{-27}\ \mathrm{kg}}}=0.9846\times10^6\ \mathrm{m/s} \tag{A.2}$$

The ion cyclotron frequency is the same for both plasmas

$$\Omega_{ci}=\frac{eB_0}{m_i}=\frac{1.6022\times10^{-19}\ \mathrm{C}\times5.74\ \mathrm{T}}{2.5\times1.67261\times10^{-27}\ \mathrm{kg}}=2.1993\times10^8\ \mathrm{Hz} \tag{A.3}$$

where the on-axis magnetic field is assumed to be $B_0=5.74$ T. Thermal ion larmor radii are

$$\rho_i(18\ \mathrm{MA})=\frac{v_{thi}(18\ \mathrm{MA})}{\Omega_{ci}}=\frac{0.8754\times10^6\ \mathrm{m/s}}{2.1993\times10^8\ \mathrm{Hz}}=0.3980\times10^{-2}\ \mathrm{m}\approx0.4\ \mathrm{cm} \tag{A.4}$$

$$\rho_i(20\ \text{MA}) = \frac{v_{thi}(20\ \text{MA})}{\Omega_{ci}} = \frac{0.9846\times10^{6}\ \text{m/s}}{2.1993\times10^{8}\ \text{Hz}} = 0.4477\times10^{-2}\ \text{m} \approx 0.45\ \text{cm} \tag{A.5}$$

The average radius of the q=1 surface is [25]

$$\bar{r}_1 \approx \sqrt{\kappa_1} r_1 a \approx \sqrt{\kappa_{egde}} \times 0.81 \times 2.9 = 2.35 \times \sqrt{1.7} = 3.06\ \text{m} \tag{A.6}$$

Note that the elongation of $\kappa_1 \approx \kappa_{egde} = 1.7$ is a reasonable estimate here, due to the flat q profile with the q=1 surface being close to the plasma boundary ($r_1 \sim 0.81$). Next, we calculate the normalized thermal ion Larmor radii for both plasmas

$$\hat{\rho}(18\ \text{MA}) = \frac{\rho_i(18\ \text{MA})}{\bar{r}_1} = \frac{0.4\ \text{cm}}{3.06\ \text{cm}} = 1.3\times10^{-3} \tag{A.7}$$

$$\hat{\rho}(20\ \text{MA}) = \frac{\rho_i(20\ \text{MA})}{\bar{r}_1} = \frac{0.45\ \text{cm}}{3.06\ \text{cm}} = 1.5\times10^{-3} \tag{A.8}$$

The thermal ion diamagnetic frequency, $\omega_*^{thi} = \left(v_{thi}/r_p\right)\hat{\rho} = T/eB_0 r_P \bar{r}_1$, depends on the plasma temperature

$$\omega_*^{thi}(18\ \text{MA}) = \frac{T_i^{18}}{eB_0 r_P \bar{r}_1} = \frac{2\times10^{4}\ \text{eV}}{5.74\ \text{T}\times0.43\ \text{m}\times3.06\ \text{m}} = 2.648\times10^{3}\ \text{s}^{-1} \tag{A.9}$$

$$\omega_*^{thi}(20\ \text{MA}) = \frac{T_i^{20}}{eB_0 r_P \bar{r}_1} = \frac{2.53\times10^{4}\ \text{eV}}{5.74\ \text{T}\times0.4\ \text{m}\times3.06\ \text{m}} = 3.601\times10^{3}\ \text{s}^{-1} \tag{A.10}$$

The equilibrium pressure scale length at the q=1 surface, $r_p = \left|dp_i/dr\right|^{-1} p_i$, is estimated as $r_p \approx 0.43\ \text{m}$ for the 18 MA scenario and $r_p \approx 0.4\ \text{m}$ for the 20 MA scenario. The Alfven time is

$$\tau_{\text{A}} = \frac{\sqrt{3}R_0}{v_{\text{A}}} = \frac{\sqrt{3}\times8.9\ \text{m}}{7.918\times10^{6}\ \text{m/s}} \approx 1.9468\times10^{-6}\ \text{s} = 1.9468\ \mu\text{s} \tag{A.11}$$

All the above factors help to establish the asymptotic limits where the layer physics effect becomes important

$$-\delta\hat{W}_c(18\ \text{MA}) \equiv \max\{\hat{\rho},\ \omega_*^{thi}\tau_A/2\} = \max\{1.3\times10^{-3},\ 2.6\times10^{-3}\} = 2.6\times10^{-3} \tag{A.12}$$

$$-\delta\hat{W}_c(20\ \text{MA}) \equiv \max\{\hat{\rho},\ \omega_*^{thi}\tau_A/2\} = \max\{1.5\times10^{-3},\ 3.5\times10^{-3}\} = 3.5\times10^{-3} \tag{A.13}$$

References

[1] Zohm H 1996 Plasma Phys. Control. Fusion **38** 105

[2] Loarte A *et al* 2007 Nucl. Fusion **47** S203-S263

[3] Wenninger R P *et al* 2014 Nucl. Fusion **54** 114003

[4] Siccinio M *et al* 2020 Fusion Eng. Design **156** 111603

[5] Evans T E *et al* 2004 Phys. Rev. Lett. **92** 235003

[6] Jeon Y M *et al* 2012 Phys. Rev. Lett. **109** 035004

[7] Sun Y *et al* 2016 Phys. Rev. Lett. **117** 115001

[8] Garofalo A M *et al* 2011 Nucl. Fusion **51** 083018

[9] Liu F *et al* 2018 Plasma Phys. Control. Fusion **60** 014039

[10] Whyte D G *et al* 2010 Nucl. Fusion **50** 105005

[11] Silvagni D, Eich T, Faitsch M, Happel T, Sieglin B, David P, Nille D, Gil L, Stroth U 2020 Plasma Phys. Control. Fusion **62** 045015

[12] Medvedev S Y *et al* 2015 Nucl. Fusion **55** 063013

[13] Austin M E *et al* 2019 Phys Rev Lett **122** 115001

[14] Kikuchi M *et al* 2019 Nucl. Fusion **59** 056017

[15] Sauter O *et al* 2014 Phys. Plasmas **21** 055906

[16] Ren J, Liu Y, Liu Y, Medvedev S Y, Wang Z, Xia G 2016 Plasma Phys. Control. Fusion **58** 115009

[17] Ren J, Liu Y, Liu Y, Medvedev S Y 2018 Nucl. Fusion **58** 126017

[18] Xue L, Zheng G Y, Duan X R, Liu Y Q, Hoang G T, Li J X, Dokuka V N, Lukash V E, Khayrutdinov R R 2019 Fusion Eng. Design **143** 48-58

[19] Camenen Y, Pochelon A, Behn R, Bottino A, Bortolon A, Coda S, Karpushov A, Sauter O, Zhuang G, team t T C V 2007 Nucl. Fusion **47** 510-516

[20] Federici G *et al* 2019 Nucl. Fusion **59** 066013

[21] Federici G *et al* 2014 Fusion Eng. Design **89** 882-889

[22] Fable E *et al* 2013 Plasma Phys. Control. Fusion **55** 124028

[23] Wu T, He H, Liu Y, Liu Y, Hao G Z, Zhu J 2018 Phys. Plasmas **25** 052504

[24] Bondeson A, Bussac M N 1992 Nucl. Fusion **32** 513

[25] Porcelli F, Boucher D, Rosenbluth M N 1996 Plasma Phys. Control. Fusion **38** 2163–2186

[26] Wu T, Liu Y, Liu Y, Zhou L, He H 2019 Phys. Plasmas **26** 102102

[27] Campbell D J *et al* 1988 Phys. Rev. Lett. **60** 2148-2151

[28] White R B, Rutherford P H, Colestock P, Bussac M N 1988 Phys. Rev. Lett. **60** 2038-2041

[29] Coppi B, Migliuolo S, Pegoraro F, Porcelli F 1990 Physics of Fluids B: Plasma Physics **2** 927-943

[30] Zhou L, Liu Y, Siccinio M, Fable E, Wu T, Duan P, Chen L 2020 Nucl. Fusion **60** 126011

[31] Martynov A, Graves J P, Sauter O 2005 Plasma Phys. Control. Fusion **47** 1743-1762

[32] Liu Y, Chu M S, Chapman I T, Hender T C 2008 Phys. Plasmas **15** 112503

[33] Liu Y Q, Bondeson A, Fransson C M, Lennartson B, Breitholtz C 2000 Phys. Plasmas **7** 3681-3690

[34] Nave M F F, Gorelenkov N N, McClements K G, Allfrey S J, Balet B, Borba D N, Lomas P J, Manickam J, Jones T T C, Thomas P R 2002 Nucl. Fusion **42** 281

[35] Liu Y, Kirk A, Nardon E 2010 Phys. Plasmas **17** 122502

[36] Berkery J W, Liu Y Q, Wang Z R, Sabbagh S A, Logan N C, Park J-K, Manickam J, Betti R 2014 Phys. Plasmas **21** 052505

[37] Wang Z, Park J-K, Liu Y, Logan N, Kim K, Menard J E 2014 Phys. Plasmas **21** 042502

[38] Liu Y, Chu M S, Chapman I T, Hender T C 2009 Nucl. Fusion **49** 035004

[39] Liu Y 2010 Nucl. Fusion **50** 095008
[40] Liu Y *et al* 2010 Plasma Phys. Control. Fusion **52** 104002
[41] Menard J E, Wang Z, Liu Y, Bell R E, Kaye S M, Park J K, Tritz K 2014 Phys. Rev. Lett. **113**
[42] Wang Z R, Lanctot M J, Liu Y Q, Park J K, Menard J E 2015 Phys. Rev. Lett. **114** 145005
[43] Hu B, Betti R, Manickam J 2006 Phys. Plasmas **13** 112505
[44] Sirén P, Varje J, Weisen H, Giacomelli L, Ho A, Nocente M 2019 Fusion Eng. Design **146** 1587-1590
[45] Gaffey J D, Jr 1976 Journal of Plasma Physics **16** 149-169
[46] Bussac M N, Pellat R, Edery D, Soule J L 1975 Phys. Rev. Lett. **35** 1638-1641
[47] C. Wahlberg a A B 2000 Phys. Plasmas **7** 923
[48] Wang F, Fu G Y, Breslau J A, Tritz K, Liu J Y 2013 Phys. Plasmas **20** 072506
[49] Liu Y, Kirk A, Gribov Y, Gryaznevich M P, Hender T C, Nardon E 2011 Nucl. Fusion **51** 083002
[50] Chapman I T, Brown S, Kemp R, Walkden N R 2012 Nucl. Fusion **52** 042005
[51] Waelbroeck F L 1996 Phys. Plasmas **3** 1047-1053
[52] Liu Y, Chapman I T, Graves J P, Hao G Z, Wang Z R, Menard J E, Okabayashi M, Strait E J, Turnbull A 2014 Phys. Plasmas **21** 056105